

Statistical Model of Exotic Rotational Correlations in Emergent Space-Time

Craig Hogan

University of Chicago and Fermilab

Ohkyung Kwon

Korea Advanced Institute of Science and Technology

Jonathan Richardson

University of Chicago and University of Michigan

A statistical model is formulated to compute exotic rotational correlations that arise as inertial frames and causal structure emerge on large scales from entangled Planck scale quantum systems. Noncommutative quantum dynamics are represented by random transverse displacements that respect causal symmetry. Entanglement is represented by covariance of these displacements in Planck scale intervals defined by future null cones of events on an observer's world line. Light that propagates in a nonradial direction inherits a projected component of the exotic rotational correlation that accumulates as a random walk in phase. A calculation of the projection and accumulation leads to exact predictions for statistical properties of exotic Planck scale correlations in an interferometer of any configuration. The cross-covariance for two nearly co-located interferometers is shown to depart only slightly from the autocovariance. Specific examples are computed for configurations that approximate realistic experiments, and show that the model can be rigorously tested.

I. INTRODUCTION

Quantum principles are widely accepted to govern all physical systems. However, there is no generally accepted theory of quantum geometry, the dynamical quantum system whose classical limit is general relativity[1–3]. Moreover, in spite of many decades of theoretical progress, no experimental technique has emerged to study exotic quantum properties of geometry itself, as distinguished from the quantum behavior of fields that inhabit classical space-time.

Quantum geometry, like any other quantum system, must produce correlations among observable quantities. The natural scale for those correlations is the Planck length $l_P \equiv \sqrt{\hbar G/c^3} = 1.616 \times 10^{-35}$ meters, where the gravitational self energy of a single quantum approaches its total energy. It is widely thought that they are not detectable, since the standard theory of quantum fields propagating in a classical background space-time[4–6] (as well as its UV completions, such as string theory[7–9]) predicts that exotic correlations from Planck length quantum gravity are negligible on laboratory scales[10]. However, this conclusion could be an artifact of approximations used to quantize fields on a classical background.

Another school of thought[1–3] holds that there is no fixed background. In such relational or emergent theories, all relationships in space and time are defined from within the geometrical quantum system. A quantum system composed of many Planck-scale elements could display much larger exotic correlations on laboratory scales than one constrained to behave as quantum field states a classical background. The system can approach a classical limit more gradually on large scales, like a Planck scale random walk, as a statistical behavior with covariances determined by the symmetries of the system. Indeed, estimates of quantum deviations from a classical system by extrapolation of standard gravity and quantum mechanics[10–16] show that they may be detectable.

Although there is an extensive literature on such relational theories, there is no generally accepted framework for how the subunits weave themselves into a whole spacetime. Large scale exotic correlation depends on how Planck scale subsystems relate to each other on large scales— that is, exactly how they are woven together. The spatial structure of their quantum entanglement determines the statistical covariance among observable operators.

This paper quantitatively analyzes observable effects in a specific model of the emergence of spatial direction in a flat space-time from a Planck scale quantum system[16]. The model accounts for the gradual emergence, in large systems, of a classical inertial nonrotating directional frame, in a system that has a complete indeterminacy of direction at the Planck scale. It is not itself a quantum theory, but a statistical model for defining rotation based on the propagation of light in an extended region of space-time. A bottom-up construction integrates the statistical effect of Planck-scale quantum elements, whose large-scale covariance is determined by classical light cones extending from every event. Propagating light inherits exotic correlations from the Planck scale that can be interpreted as rotational fluctuations in the inertial frame. In an interferometer, the layout of light paths through space uniquely determines the response to exotic correlations. Our technique predicts the full functional form of the auto- and cross- correlation of interferometer signals with only one free parameter, the fundamental coherence scale of the exotic correlation. The formulation here shows that simple principles based on causal structure fully determine the functional form for the autocorrelation

and cross correlation of any layout of interferometers, without assumptions about the specific dynamics of the Planck scale quantum subsystems. It thus forms a complete and precisely formulated phenomenological framework for a comprehensive experimental program to explore one form of relational emergent geometry. This analysis will be useful to design experiments and to interpret experimental results.

A. Experimental Probes and the Holometer Program

Experimental results already significantly constrain some forms of exotic Planck scale correlations. Observations of distant astronomical objects (e.g., quasars, AGN, gamma-ray bursts) now constrain some exotic correlations with longitudinal, or line-of-sight, symmetry to a coherence scale close to or below the Planck length [17–23]. Under such an effect, light emitted by a distant source accumulates random phase deviations while propagating between source and observer. The phase decoherence could be detectable as a distance-dependent degradation of the intensity and/or resolution of the source image, or as a dispersion in frequency space.

Exotic correlations with symmetry *transverse* to a null separation may have no dispersive effect on cosmic propagation, but still be detectable via laser interferometry[10–16]. Experimental results are now starting to significantly constrain models of this kind that are not specifically constrained to obey rotational symmetry. Fluctuations in strain are constrained to a coherence scale below the Planck length by gravitational wave experiments[10]. Exotic correlations with shear symmetry— those that can be visualized as a random walk of the interferometer beamsplitter, or of the position of a beam transverse to its direction of propagation— have not in general been previously tested to Planck-scale sensitivity, as existing gravitational wave interferometers are optimized for lower-frequency detection, corresponding to time scales much longer than the light-crossing time of the apparatus; high-fidelity constraints on time and position correlations in an extended volume of space-time require measurements sampled faster than a light-crossing time in more than one spatial direction. Tighter general constraints on shear models are now being achieved by the Fermilab Holometer [24], the first experiment specifically designed to measure exotic positional relationships in space-time at Planck sensitivity over a broad bandwidth. Prospects are good to rule out conclusively all forms of exotic shear[10, 15] that agree with the Planck normalization predicted from gravitation.

The exotic Planck scale correlations with rotational symmetry considered here— purely directional twists on an observer’s light cones— have not yet been tested experimentally at Planck sensitivity. The projections here show that a reconfiguration of the Holometer to a different light path that includes transverse segments should have the sensitivity to measure the effect or rule out the basic hypothesis of entanglement that underlies our model.

II. EXOTIC ROTATIONAL CORRELATIONS

A. Motivation

A classical world line is a continuous system, with an infinite amount of information, but time and space in the real world are quantized at some length ℓ_P . Thus, the information content or bandwidth of a physical world line is limited to that of a discrete 1D time series with steps of some duration ℓ_P/c , regardless of detailed dynamics. That limit applies as well to the rotational relationship of its local inertial frame with rest of the universe.

In quantum gravity, it is not clear how stable directions in space arise[16]. The Planck information limit constrains the directional relationships of an observer with the rest of the system, that is, any other world lines. A quantum foam at the Planck scale is associated with virtual Kerr black holes and frame dragging, and hence also with indeterminacy and fluctuations of spin, in particular, with Planck frequency fluctuations in direction as well as Planck length translations and displacements in time and space. The system is made of many quantum elements, each of which resembles an atomic spin, and has only about a single qubit of information about all of its spatiotemporal relationships with the rest of the universe. Thus, local inertial frames do not exist at the Planck scale, even in a flat space-time. We wish to show how stable directions in space can emerge statistically from many such elements in a large relational system, with no built-in, large-scale correlations, where each Planck scale element only passes information to elements that are adjacent to it in both space and time.

The model here introduces a specific mechanism— entanglement on light cones— that explains how a nearly classical, stable direction can emerge over a long time interval, by entanglement and averaging over many elements. The structure of the averaging is determined by the emergent classical causal structure defined by light cones from the events on an observer’s world line. The directional resolution is still limited because of the limited information, so the inertial frame fluctuates by a tiny amount on large scales from the absolute classical frame. The scale of these exotic rotational correlations can be estimated from several different extrapolations of standard quantum mechanics and gravity[16], such as wave mechanics, spin algebra, field theory, diffusion, or statistical random walks, which describe

the projection of a 1D time series onto two dimensions of direction. The estimated effect can be expressed as a variance in transverse position and direction at distance R :

$$\langle X_{\perp}^2 \rangle_R = \ell_P R, \quad (1)$$

$$\langle \Delta\theta^2 \rangle_R = \ell_P / R, \quad (2)$$

with a normalization approximately equal to the standard Planck length, $\ell_P \approx l_P$. The emergent system displays exotic rotations—fluctuations or “twists” in the inertial frame—that correspond to displacements of this magnitude on a timescale R/c . These fluctuations could have observable effects on propagating light.

The quantitative model here analyzes the mathematical elements of this picture much more sharply than the physical scenario for emergence of inertial frames sketched in ref.[16]. We present an operational definition of rotation—in effect, a concrete covariant, operational model of quantum measurement for an emergent geometry. This model captures details of the unique constraints imposed by preserving exact causal structure at Planck resolution, and allows us to make exact predictions for exotic statistical correlations in experiments with only one parameter, the Planck correlation scale ℓ_P .

B. Assumptions

We start from the idea that an entire physical system, including space and time, obeys quantum mechanics. Space and time are relational, that is, all spatial relationships are derived within a quantum system made of elements or subsystems at the Planck scale. The relative positions of what emerge as classical events are associated with how the Planck scale elements entangle to produce a whole system. Quantum decoherence leads to random Planck length displacements between elements, modeled as classical random variables. Entanglement of the elements produces correlations, expressed in our model as a covariance among the random variables. The covariance is confined to within a Planck length of future light cones defined by each event on the world line of an observer. This structure is used to derive the exotic large scale correlations of observables. As light propagates through this system it entangles with the geometrical state and inherits a projection of the exotic Planck scale phase correlation. The difference from classical behavior manifests as an exotic “spooky” correlation of the phase of the light, not present in standard theory. It can affect the signal in an instrument that measures a difference in phase from two different paths, such as an interferometer. The statistical result depends only on the shape of the light path, although the actual noise signal depends on the world line where the phases are converted into a signal—the “collapse” of the wave function of the space-time in a particular situation.

The model has no dynamics, but is based only on statistics and classical geometry. This generic model of correlations shows how Planck scale quantum elements can entangle to create emergent classical inertial frames, in a way that is highly constrained by known symmetries of causal structure. The correlations quantitatively describe the relationship between local and global inertial frames—the quantum deviations from the classical Machian agreement between local and global measures of rotation. They account for how chaotic and indeterminate directions at the Planck scale can emerge to approximate a determinate classical space-time on large scales.

C. Covariance of Random Displacement on Future Light Cones of an Observer

Light cones (or null cones) are the covariant objects that define causal structure; they define the sharp classical boundaries between past, present and future, and between timelike and spacelike separation of events. We base our model on the principle that classical causal structure is respected on all scales larger than the Planck length. In the frame of an observer O , we define a “light cone time” coordinate variable,

$$\mathbb{T}_O = t_O - \frac{|\mathbf{x}_O|}{c}. \quad (3)$$

A surface of constant \mathbb{T} in 3+1D represents a 2+1D light cone emanating from an event on an observer’s world line, a 3-surface defined in conventional coordinates by $t = |\mathbf{x}|/c$. Although we will choose to calculate in the rest frame of an observer, the causal relationships defined by the actual light cones are independent of the choice of frame and have a Lorentz invariant physical meaning. In the following, we drop subscripts until they are needed later for comparing measurements from more than one observer.

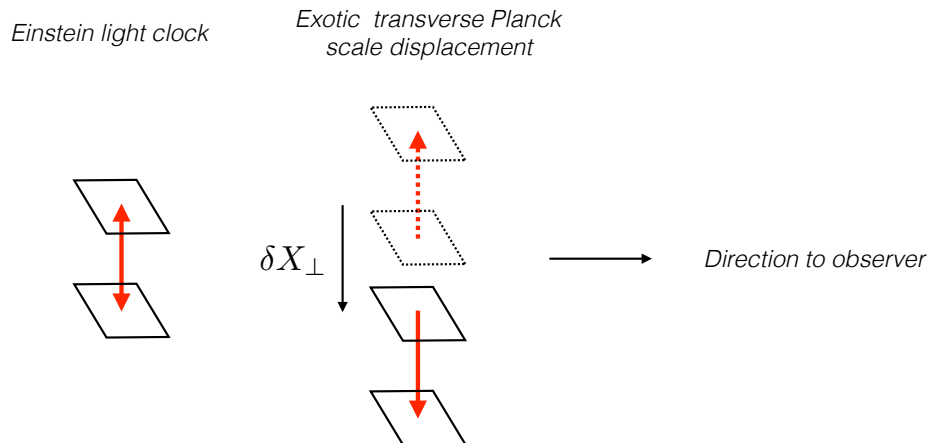


FIG. 1. A macroscopic space-time can be built out of local relationships among quantum elements, shown here schematically at the Planck scale. Unlike a classical Einstein clock with light bouncing between two mirrors, positions in a relational geometry do not commute with each other. A projection in one direction creates a superposition of position in the transverse directions, giving rise to a random Planck scale displacement from quantum noise when measurements in those directions collapse the wave function. Translation along a null direction in time creates an eigenstate in the radial spatial direction from any observer, which leads to classical causal structure. The transverse displacement collapses into the same state in all directions from an observer, for light cone time separations smaller than a Planck length. Those displacements also affect the phase of transversely-propagating light, as shown schematically here by red arrows for two ticks of a Planck scale light clock.

To connect with physical observables we develop a model of the geometrical character of random variables, which will allow us to compute how the random displacements affect physical quantities. The exotic departure from the classical system is described as a random variable with variance ℓ_P^2 :

$$\delta X_{\perp}(\mathbb{T}) \sim \mathcal{N}(0, \ell_P^2). \quad (4)$$

The transverse displacement variable δX_{\perp} represents an exotic displacement relative to the classical inertial frame, normal to the direction to the observer. It has zero mean so the large scale average is classical. In our model it is interpreted physically as a displacement of phase for transversely propagating light, but should be regarded as a modification of classical position of space itself, and everything in it, relative to the observer (see Fig. 1). The coherence scale and randomness model the effect of the finite information content of the indeterminate quantum elements that make up the relational space-time. Since the physical effects are purely transverse, the model exactly preserves causal structure, an assumed exact symmetry of quantum gravity.

In a discrete description with the same information content, this quantity corresponds to an exotic incremental displacement at each discrete step—a random step of length ℓ_P each timestep t_P , due the noncommutativity of discrete quantum geometrical operators. All of the predictions below have only one parameter, ℓ_P , which, to be consistent with a discrete description and exact causal symmetry, denotes both the coherence length of the quantum elements and the magnitude of random displacements. A non-zero value of ℓ_P results in a finite, countable information content, and introduces deviations from classical continuous space-time. Based on extrapolation of gravity and quantum mechanics[10–16], its value should be approximately the Planck length l_P .

We now introduce the new, central hypothesis of this paper, the part of the model that encapsulates the relationship of Planck scale quantum elements to each other and to an observer on large scales (see Fig. 2). That hypothesis can be written as a covariance of an exotic displacement on future light cones:

$$\text{cov}(\delta X_{\perp}(\mathbb{T}'), \delta X_{\perp}(\mathbb{T}'')) = \begin{cases} \ell_P^2, & |\mathbb{T}' - \mathbb{T}''| < \frac{1}{2}t_P \\ 0, & \text{otherwise} \end{cases} \quad (5)$$

For calculational convenience and clarity, in place of a discrete model of time steps, or a continuous Gaussian roll-off (say), the model uses sharply delineated bins of constant covariance in \mathbb{T} ; none of the results depend on this choice.

Physically, this hypothesis is motivated by the emergent scenario summarized above. The physical effects of each quantum element are entirely local, confined to adjacent quantum elements—those within one Planck length or time. Thus, they are consistent with a theory of quantum gravity in which the space-time system as a whole emerges entirely

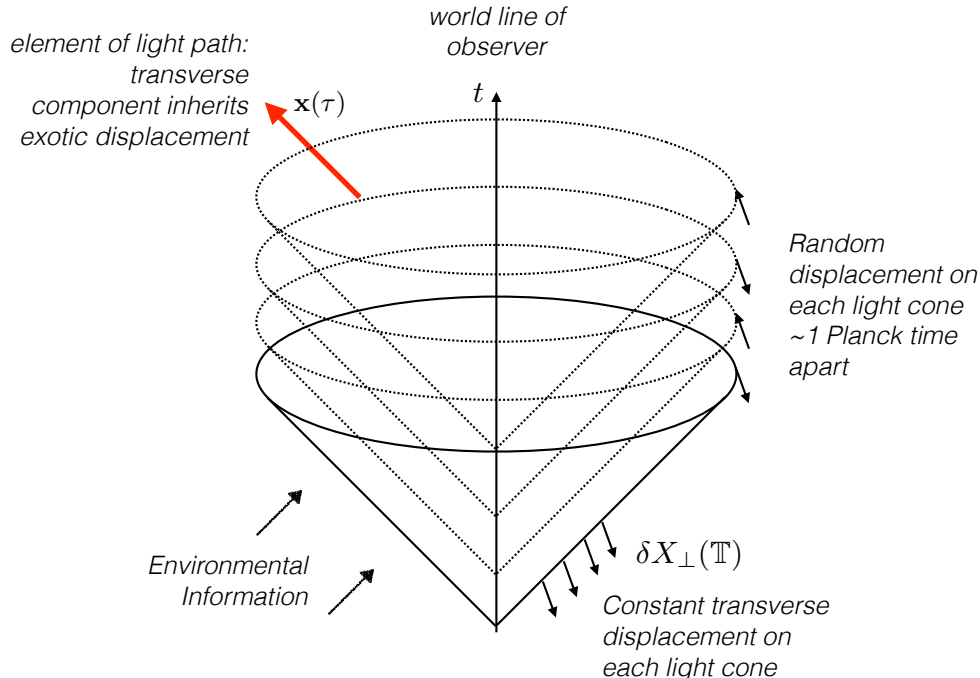


FIG. 2. Classical picture of the causal structure of large scale covariances in exotic space-time positional relationships. Space and time are shown in the observer’s frame, with one spatial dimension suppressed. A series of light cones, surfaces of constant light cone time \mathbb{T} , is shown emerging from an observer’s world line. These determine the space-time structure of correlations produced by Planck scale entanglement. Within a Planck length of each surface of constant \mathbb{T} , the same random transverse spatial displacement or “quantum twist” $\delta X_{\perp}(\mathbb{T})$ of about a Planck length— a consequence of noncommutative geometry at the Planck scale— is causally inherited by entanglement with a quantum state prepared on the observer’s world line. Thus, entanglement is causally local: each event on the observer’s world line determines the projection of all future events that lie within a Planck length of null separation. Propagating light inherits the projection of the local transverse displacement onto its path $\mathbf{x}(\tau)$. The total effect on the light phase is an accumulation of projected components of random displacements from crossing a series of light cones. Transverse displacements accumulate like a random walk and lead to a mean square displacement much larger than the Planck length.

from the relationships among these parts, without any fixed background reference space. Furthermore, events that are separated by light cone times smaller than the coherence length have correlated transverse displacements. The choice of an observer’s world line determines its entanglement with Planck scale elements everywhere, in a Lorentz invariant way. The time sequence of Planck scale quantum states on an observer’s world line broadcast to the future in every direction at a finite information density, the Planck bandwidth. These local correlations then lead statistically to a stable, organized global structure.

Although we call the displacements “quantum twists,” note that the variable represents a constant transverse displacement, and not a constant angle, everywhere on the light cone. The correlations which result from entanglement appear spooky, since they appear nonlocally across spacelike hypersurfaces, but they are still local in the sense that they are determined by sub-Planck light cone time separation between events. Causal relationships determine the collapse of the quantum state into classical random observables.

Heuristically, although directions at the Planck length are highly uncertain (and fluctuate by a radian per Planck time), from the macroscopic perspective, nearly classical directions emerge in a large scale average. The direction to an event at distance R can be encoded by $\approx (R/\ell_P)$ qubits. Directions to distant objects are not independent, but are entangled with each other. Every Planck step along an observer’s world line represents a new binary random choice of “which direction to look.” Information from each event on the world line prepares the state and entangles the projection of the displacement operators at all events on the future light cone. The random variable is a classical shorthand for quantum decoherence, and the covariance is a classical shortcut to describe quantum entanglement

among the individual Planck scale elements: events on a light cone must “agree on” the projection of the corresponding spin state onto any given axis. In the plane of an interferometer, every point on a light cone steps clockwise or counterclockwise by one Planck length from the previous one. Apparently non-local spatial correlations arise from causal entanglement of the Planck scale degrees of freedom.

It will prove further convenient to define a *rate* of transverse position fluctuation, or an effective transverse “velocity” or jitter,

$$\frac{dX_{\perp}(\mathbb{T})}{d\mathbb{T}} \equiv \frac{\delta X_{\perp}(\mathbb{T})}{t_P} \quad (6)$$

This quantity is not a physical velocity or momentum, but represents a discrete “motion” of the Planck scale quantum elements whose symmetry gives rise to emergent causality. It is explicitly dependent only on \mathbb{T} (and not individually on t or \mathbf{x}) due to the coherence of the fluctuations on light cones. This variable is distributed as

$$\frac{dX_{\perp}(\mathbb{T})}{d\mathbb{T}} \sim \mathcal{N}\left(0, \left(\frac{\ell_P}{t_P}\right)^2\right) \quad (7)$$

with the covariance structure

$$\text{cov}\left(\frac{dX_{\perp}}{d\mathbb{T}}(\mathbb{T}'), \frac{dX_{\perp}}{d\mathbb{T}}(\mathbb{T}'')\right) = \begin{cases} \left(\frac{\ell_P}{t_P}\right)^2, & |\mathbb{T}'' - \mathbb{T}'| < \frac{1}{2}t_P \\ 0, & \text{otherwise} \end{cases} \quad (8)$$

The characteristic rate of a transverse position random walk is thus one coherence length per coherence time, or c .

III. EXOTIC CORRELATIONS IN INTERFEROMETER SIGNALS

We now estimate the effect of exotic displacements on measurable phase shifts in beams of freely-propagating light. These phase shifts are measured by an interferometer consisting of a beamsplitter and two or more reflecting mirrors. Light from a coherent source is split into two beams which propagate through an arrangement of mirrors and back to the beamsplitter, where they recombine. Any difference in the distance propagated by the two beams introduces a corresponding difference in the accumulated optical phase. Interference effects from this phase difference modulate the power of the recombined beam, which is read out via a photodetector at the output, or antisymmetric port of the instrument. In this section, the general response of an interferometer to exotic rotational displacements will be derived. In spite of the simple and symmetric form of the fundamental exotic covariance, the projection onto observables is surprisingly subtle. These results will be used below to compute the instrument response of specific configurations of mirrors.

A. Effect of Exotic Displacements on the Signal

We model the effect of exotic displacements on an idealized interferometer. Propagating light encounters a beamsplitter and divides into two separate paths, 1 and 2, of equal expected length. The power at the antisymmetric port is exquisitely sensitive to the difference in path lengths[25]. A time series of measurements is represented by

$$S(t) \equiv S_2(t) - S_1(t). \quad (9)$$

Here S_1 and S_2 represent the optical path lengths (OPL) of the two arms and S represents the optical path difference (OPD), in the inertial frame of the beamsplitter, and t denotes laboratory time.

We now show how the exotic fluctuations manifest as random deviations from the classical OPL. The two classical optical paths will be parameterized by propagation time $\tau \in [0, \mathcal{T}]$, where \mathcal{T} is the full duration of the optical phase measurement, twice the length of each path. At propagation time τ , the classical position of a tracer photon traversing path i will be denoted by $\mathbf{x}_i(\tau)$. These tracer photons do not represent actual quanta of localized energy, but rather null propagation in the inertial frame. At every point along optical path $\mathbf{x}_{1,2}(\tau)$, there exists a unit vector tangent to the path, $\hat{\mathbf{x}}_{1,2}(\tau)/c \equiv d\mathbf{x}_{1,2}(\tau)/cd\tau$. This unit vector represents the instantaneous direction of light travel through interferometer.

The light origin, $\mathbf{x}_1(0) = \mathbf{x}_2(0)$, provides a common reference for the optical phase measurement made by either path. It can thus be regarded, under a relational theory, as a fixed reference point against which all other points

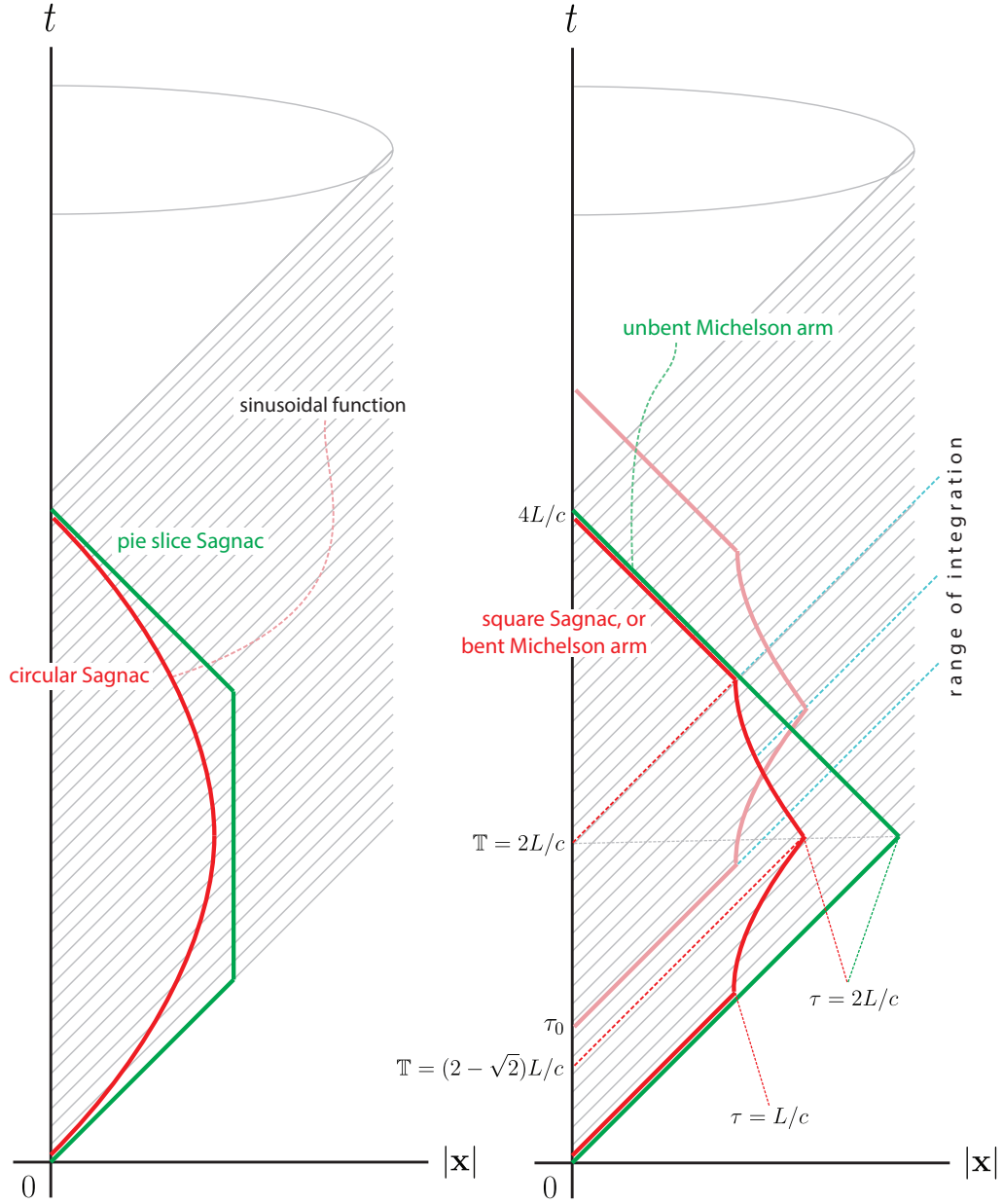


FIG. 3. How quantum twists of the inertial frame project onto an interferometer signal. Laboratory time is plotted against radial position in the observer frame, with the two transverse spatial dimensions suppressed, so each point represents a 2-sphere at a single time. A sequence of future light cones (constant \mathbb{T} surfaces) is shown for the same observer. Light paths are shown for various interferometer configurations. As a path crosses each light cone, a projection of transverse displacement is added, that accumulates as a random walk and eventually appears as a detectable difference in phase. Note that although the outbound and inbound paths are spatially symmetric in laboratory time, their contribution to exotic correlation is not symmetric in measured signal lag, because the opposite sign for the radial part of their propagation changes the rate at which they cross outbound light cones and thereby accumulate variance. On the right, the red path is shown at two different beamsplitter reflection times, along with the corresponding range of integration for time lag τ_0 .

in space appear to fluctuate. For each path, the optical distance propagated by the tracer photon over a classical light-crossing time is given by the path integral

$$S_{1,2}(t + \mathcal{T}) = \int_t^{t+\mathcal{T}} \left[\dot{\mathbf{x}}_{1,2}(t' - t) + \dot{X}_\perp(\mathbb{T}(t', \mathbf{x}_{1,2}(t' - t))) \hat{\boldsymbol{\theta}} \right] \cdot \frac{\dot{\mathbf{x}}_{1,2}(t' - t)}{c} dt', \quad (10)$$

where

$$\dot{X}_\perp(\mathbb{T}(t, \mathbf{x})) \equiv \frac{d}{dt} X_\perp(\mathbb{T}(t, \mathbf{x})) = \frac{dX_\perp(\mathbb{T})}{d\mathbb{T}} \frac{d\mathbb{T}(t, \mathbf{x})}{dt} \quad (11)$$

is the rate of transverse exotic displacement per propagation time. These displacements occur in the direction transverse to radial separation from the observer's world line, a unit vector in the interferometer plane we denote by $\hat{\boldsymbol{\theta}}$. The vector sum of this rate and the classical velocity corresponds to the "effective" velocity of the tracer photon relative to the classical spatial coordinates. The instantaneous effect on the OPL is obtained by taking the component of this effective velocity in the direction of light travel.

Under the variable substitution $\tau \equiv t' - t$, eq. 10 becomes

$$S_{1,2}(t + \mathcal{T}) = \int_0^{\mathcal{T}} \left[\dot{\mathbf{x}}_{1,2}(\tau) + \dot{X}_\perp(\mathbb{T}(t + \tau, \mathbf{x}_{1,2}(\tau))) \hat{\boldsymbol{\theta}} \right] \cdot \frac{\dot{\mathbf{x}}_{1,2}(\tau)}{c} d\tau \quad (12)$$

$$= \int_0^{\mathcal{T}} \left[c \hat{\mathbb{T}}_{1,2}(\tau) + \frac{dX_\perp(\mathbb{T})}{d\mathbb{T}} \frac{d\mathbb{T}}{d\tau}(\tau, \mathbf{x}_{1,2}(\tau)) \hat{\boldsymbol{\theta}} \right] \cdot \frac{\dot{\mathbf{x}}_{1,2}(\tau)}{c} d\tau \quad (13)$$

$$= c\mathcal{T} + \int_0^{\mathcal{T}} \frac{dX_\perp(\mathbb{T})}{d\mathbb{T}} \mathcal{P}_{1,2}(\tau) d\tau \quad (14)$$

Here we use the fact that $d\mathbb{T}/dt' = d\mathbb{T}/d\tau$ and independent of t , referring to the definition in eq. 3, and define

$$\mathcal{P}_{1,2}(\tau) \equiv \left[\frac{d\mathbb{T}}{d\tau}(\tau, \mathbf{x}_{1,2}(\tau)) \right] \left[\hat{\boldsymbol{\theta}} \cdot \frac{\dot{\mathbf{x}}_{1,2}(\tau)}{c} \right] \quad (15)$$

$$= \left(1 - \frac{1}{c} \frac{d|\mathbf{x}_{1,2}|}{d\tau} \right) \left(\hat{\boldsymbol{\theta}} \cdot \frac{1}{c} \frac{d\mathbf{x}_{1,2}}{d\tau} \right) \quad (16)$$

$$= \left(1 - \frac{v_r}{c} \right)_{1,2} \left(\frac{v_\theta}{c} \right)_{1,2} \quad (17)$$

as a projection factor that captures all the dependence on the light path of a specific interferometer configuration. The meaning of this factor becomes conceptually clear when we write $\mathbf{x} = (r, \theta, z)$ in polar coordinates, and denote $\dot{\mathbf{x}} = (\dot{r}, r\dot{\theta}, \dot{z}) = (v_r, v_\theta, v_z)$. The first half, $d\mathbb{T}/d\tau$, is the rate of spacetime propagation relative to outgoing radial null surfaces ($r/ct = 1$), or equivalently, the number of independently fluctuating light cones that the light path slices through per propagation time (see Figure 3). Its value is 0 when the propagation is purely radial in the outgoing direction, 1 when it is purely angular, and 2 when it is purely radial in the incoming direction. This part is a projection in the 1+1D space of (t, r) . On the other hand, the second half, $\hat{\boldsymbol{\theta}} \cdot \dot{\mathbf{x}}/c$, is a projection in the 2D space of (r, θ) . It is simply the component of the exotic displacement that is spatially tangential to the light path.

In this form, the spatial fluctuations accumulated over a measurement duration can be clearly seen to manifest as a deviation from the classical OPL. The difference of optical distances along two paths then yields the exotic effect on the OPD,

$$S(t + \mathcal{T}) = \int_0^{\mathcal{T}} \frac{dX_\perp}{d\mathbb{T}}(\mathbb{T}(t + \tau, \mathbf{x}_2(\tau))) \mathcal{P}_2(\tau) d\tau - \int_0^{\mathcal{T}} \frac{dX_\perp}{d\mathbb{T}}(\mathbb{T}(t + \tau, \mathbf{x}_1(\tau))) \mathcal{P}_1(\tau) d\tau \quad (18)$$

The geometrical projection factor $\mathcal{P}_{1,2}(\tau)$ determines the statistical response of an instrument of arbitrary geometry.

B. Single-Interferometer Statistics

Eq. 18 represents OPD measurements made over an interval of time as a set of random variables indexed by measurement time t . It is a straightforward, if somewhat complicated exercise to calculate the general statistical moments of this measurement set in the presence of exotic spatial fluctuations.

The expected value of an OPD measurement is

$$\langle S(t) \rangle = \left\langle \sum_a^{1,2} (-1)^a \int_0^{\mathcal{T}} \frac{dX_\perp}{d\mathbb{T}}(\mathbb{T}(\tau + (t - \mathcal{T}), \mathbf{x}_a(\tau))) \mathcal{P}_a(\tau) d\tau \right\rangle \quad (19)$$

$$= \sum_a^{1,2} (-1)^a \int_0^{\mathcal{T}} \left\langle \frac{dX_\perp(\mathbb{T})}{d\mathbb{T}} \right\rangle \mathcal{P}_a(\tau) d\tau \quad (20)$$

$$= 0, \quad (21)$$

using the additive separability of expectation values. The zero mean of the measurement is seen to be a direct consequence of the zero-mean process generating the spatial fluctuations, independent of the geometry of the apparatus.

The autocovariance of two OPD measurements separated in time by τ_0 is

$$C_{SS}(\tau_0 | \ell_P) \equiv \langle S(t) S(t + \tau_0) \rangle - \langle S(t) \rangle \langle S(t + \tau_0) \rangle \quad (22)$$

$$= \sum_{a,b}^{1,2} (-1)^{a+b} \left\langle \int_0^{\mathcal{T}} \frac{dX_{\perp}}{d\mathbb{T}} (\mathbb{T}(\tau' + (t - \mathcal{T}), \mathbf{x}_a(\tau'))) \mathcal{P}_a(\tau') d\tau' \right. \\ \left. \times \int_{\tau_0}^{\mathcal{T}+\tau_0} \frac{dX_{\perp}}{d\mathbb{T}} (\mathbb{T}(\tau'' + (t - \mathcal{T}), \mathbf{x}_b(\tau'' - \tau_0))) \mathcal{P}_b(\tau'' - \tau_0) d\tau'' \right\rangle \quad (23)$$

$$= \sum_{a,b}^{1,2} (-1)^{a+b} \int_0^{\mathcal{T}} d\tau' \mathcal{P}_a(\tau') \int_{\tau_0}^{\mathcal{T}+\tau_0} d\tau'' \mathcal{P}_b(\tau'' - \tau_0) \\ \times \left\langle \frac{dX_{\perp}}{d\mathbb{T}} (\mathbb{T}(\tau', \mathbf{x}_a(\tau'))) \frac{dX_{\perp}}{d\mathbb{T}} (\mathbb{T}(\tau'', \mathbf{x}_b(\tau'' - \tau_0))) \right\rangle \quad (24)$$

$$= \sum_{a,b}^{1,2} (-1)^{a+b} \int_0^{\mathcal{T}} d\tau' \frac{d\mathbb{T}}{d\tau'} (\tau', \mathbf{x}_a(\tau')) \Theta_a(\tau') \int_{\tau_0}^{\mathcal{T}+\tau_0} d\tau'' \frac{d\mathbb{T}}{d\tau''} (\tau'', \mathbf{x}_b(\tau'' - \tau_0)) \Theta_b(\tau'' - \tau_0) \\ \times \left\langle \frac{dX_{\perp}}{d\mathbb{T}} (\mathbb{T}(\tau', \mathbf{x}_a(\tau'))) \frac{dX_{\perp}}{d\mathbb{T}} (\mathbb{T}(\tau'', \mathbf{x}_b(\tau'' - \tau_0))) \right\rangle \quad (25)$$

The first step (Eq. 23) follows from the vanishing mean just derived; in the second step, the statistical terms are collected together; and in the third step (Eq. 25), projection factors are separated to reduce the integration to a single light cone time variable. We then take a final step (Eq. 26) that invokes the covariance structure of the displacements. The integral is evaluated only in the Planck-size bins where the covariance is not zero, a criterion that determines an inverse function that maps light cone time onto the laboratory time of the corresponding part of the measured signal:

$$C_{SS}(\tau_0 | \ell_P) \approx \sum_{a,b}^{1,2} (-1)^{a+b} c \ell_P \int_{|\tau_0|}^{\mathcal{T}} \Theta_a(\xi_a(\mathbb{T}, 0)) \Theta_b(\xi_b(\mathbb{T}, |\tau_0|) - |\tau_0|) d\mathbb{T}, \quad (26)$$

where we separate out just the spatial part of the projection factor $\mathcal{P}_{1,2}(\tau)$ as

$$\Theta_{1,2}(\tau) \equiv \hat{\boldsymbol{\theta}} \cdot \frac{\dot{\mathbf{x}}_{1,2}(\tau)}{c} \quad (27)$$

and $\xi_{1,2}$ is an inverse function for $\mathbb{T}(t, \mathbf{x})$ defined such that

$$\tau' = \xi_{1,2}(\mathbb{T}, 0) \quad \text{when} \quad \mathbb{T} = \mathbb{T}(\tau', \mathbf{x}_{1,2}(\tau')) \quad (28)$$

$$\tau'' = \xi_{1,2}(\mathbb{T}, \tau_0) \quad \text{when} \quad \mathbb{T} = \mathbb{T}(\tau'', \mathbf{x}_{1,2}(\tau'' - \tau_0)). \quad (29)$$

The inverse function is well-defined everywhere except when $\mathbf{x}_{1,2}$ is purely radial in the outgoing direction, where \mathbb{T} is constant over a null path (everywhere else, \mathbb{T} is monotonically increasing). However, over those segments, $\Theta_{1,2} = 0$, making those parts irrelevant. The last step (Eq. 26) should be a highly accurate approximation mathematically; the Planck scale is almost infinitesimal for practical purposes. However, since we treat the covariance structure $\langle dX_{\perp}/d\mathbb{T} dX_{\perp}/d\mathbb{T} \rangle$ as providing bins of Planck length width, our spacetime is not continuous but discrete at the Planck scale. Formally the integral picks out a single value of $\Theta_{1,2}$ for each bin in \mathbb{T} , instead of treating $\Theta_{1,2}$ as slowly-varying continuous functions. For nearly or exactly radial propagation, the difference can be important in numerical computations, but these regions are suppressed by near-zero values of $\Theta_{1,2}$. The mapping between \mathbb{T} and τ is nonlinear and dependent on $\mathbf{x}_{1,2}$, which means that in practice, for a specific interferometer configuration, the range of intervals for τ' and τ'' map nontrivially to an integration over \mathbb{T} . We show examples of this below.

Equations (23) to (26) specify the effect of Planck scale correlations on the signal of any interferometer. In general, the covariance does not vanish but behaves approximately like a Planck random walk for some intervals of time, for a layout where the light paths have a projected transverse component. The autocovariance identically vanishes for separations $|\tau_0|$ larger than the duration over which an individual measurement has nonzero geometrical projection $\mathcal{P}_{1,2}(\tau)$ (see Figure 3).

Under the Wiener-Khinchin theorem, an equivalent, frequency-space representation of the autocovariance is the power spectral density (PSD). The PSD is defined as the Fourier transform of the autocovariance,

$$\widetilde{C_{SS}}(f | \ell_P) \equiv 2 \int_{-\infty}^{\infty} C_{SS}(\tau_0 | \ell_P) e^{-i2\pi f \tau_0} d\tau_0 \quad (30)$$

$$= 4 \int_0^{\infty} C_{SS}(\tau_0 | \ell_P) \cos(2\pi f \tau_0) d\tau_0, \quad (31)$$

where the second equality follows from the fact that $C_{SS}(\tau_0 | \ell_P) = C_{SS}(-\tau_0 | \ell_P)$. This PSD, written in the so-called engineering convention, is defined only for positive frequencies, in which the power contained in the redundant negative frequencies is folded via the multiplicative prefactor of two.

IV. PROJECTIONS FOR EXPERIMENTAL LAYOUTS

To aid in conceptual design of experiments, and to gain insight into the character of the exotic correlations, it is useful to survey the signal response of specific interferometer configurations (see Figure 4). Two features stand out as required for detectable effect: (1) a layout where light travels a substantial distance in a direction that is not purely radial with respect to the “observer” (that is, the beamsplitter where the state is prepared); and (2) the ability to measure correlations on a timescale short compared with a light travel time in the interferometer arms, or equivalently over a frequency bandwidth comparable to the free spectral range.

The calculational framework above is designed for two optical paths labeled by 1 and 2 that eventually recombine. In the Michelson configurations, a beamsplitter sends light into two separate arms. In the Sagnac configurations[26, 27], the split light travels in opposite directions around the same path. In a Sagnac system, we consider tracer photons propagating in opposite directions and label their optical paths by 1 and 2. The formalism applies entirely unchanged in both cases. Idealized configurations, the “pie slice Sagnac” and the “circular Sagnac,” have curved light paths that can be considered as limiting cases of many short segments. They are presented as thought experiments to demonstrate statistical characteristics of the covariance structure. More realistic configurations for experimental setups are a “square Sagnac” and a “bent Michelson.” One form of the latter will be the main focus of the second phase of the Holometer program, as it is technologically simpler to implement and allows a reliable null configuration.

Throughout this section, we present our spectra normalized with respect to a system timescale \mathcal{T}_0 . This is sometimes the same as light circulation time \mathcal{T} , but often, because the light phase is not sensitive to rotational shifts when its propagation is purely radial, the effective optical path length over which there is nonzero geometrical coupling is smaller. \mathcal{T}_0 is the duration of time a tracer photon spends within these segments— for example, for the bent Michelson configuration, \mathcal{T}_0 is round trip time within the bent portion of the arm, whereas \mathcal{T} is the total round trip time.

A. Michelson Interferometer with Straight Arms

A standard Michelson interferometer, commonly used in gravitational wave observatories and in the initial phase of the Holometer experiment, has no sensitivity to the posited effect due to the fact that the light propagation is always radial with respect to the reference observer world line at the beamsplitter, making the geometrical coupling $\Theta(\tau)$ zero over the whole light paths. Some spatial element of angular propagation is necessary to have nonzero response. This property provides a useful way to design a null experiment to calibrate environmental noise and systematic errors.

B. Pie Slice Sagnac Interferometer

This is the simplest configuration to understand, with a perfectly linear time-domain spectrum that is conceptually straightforward to derive. As shown in Figure 4, it consists of two purely radial segments of equal length R , both of them with zero geometrical coupling $\Theta(\tau)$ to rotational jitter, connected by a circular arc that spans a quarter circle of radius R , over which the light propagation is purely angular and the projection factors $\mathcal{P}_{1,2}(\tau)$ take values of ± 1 . The completed loop therefore has a system timescale of just $\mathcal{T}_0 = \frac{1}{2}\pi R/c$ (despite the light circulation time being $\mathcal{T} = (\frac{1}{2}\pi + 2)R/c$), and the total accumulated correlation as a function of time lag τ_0 is:

$$C_{SS}(\tau_0 | \ell_P) = \begin{cases} 2^2 c \ell_P \mathcal{T}_0 (1 - |\tau_0|/\mathcal{T}_0), & 0 < |\tau_0| < \mathcal{T}_0 \\ 0, & \text{otherwise} \end{cases} \quad (32)$$

where the factor of 2 comes from the two optical paths each picking up the same jitter. The time-domain signal is an autocovariance of the OPD fluctuations, so the factor is squared (see Eq. 23). As the time lag τ_0 increases in magnitude, the duration of beamsplitter light cone time \mathbb{T} over which there are correlated fluctuations decreases linearly, up to the total timespan \mathcal{T}_0 over which the light propagation is angular and the light phase is sensitive to rotational shifts.

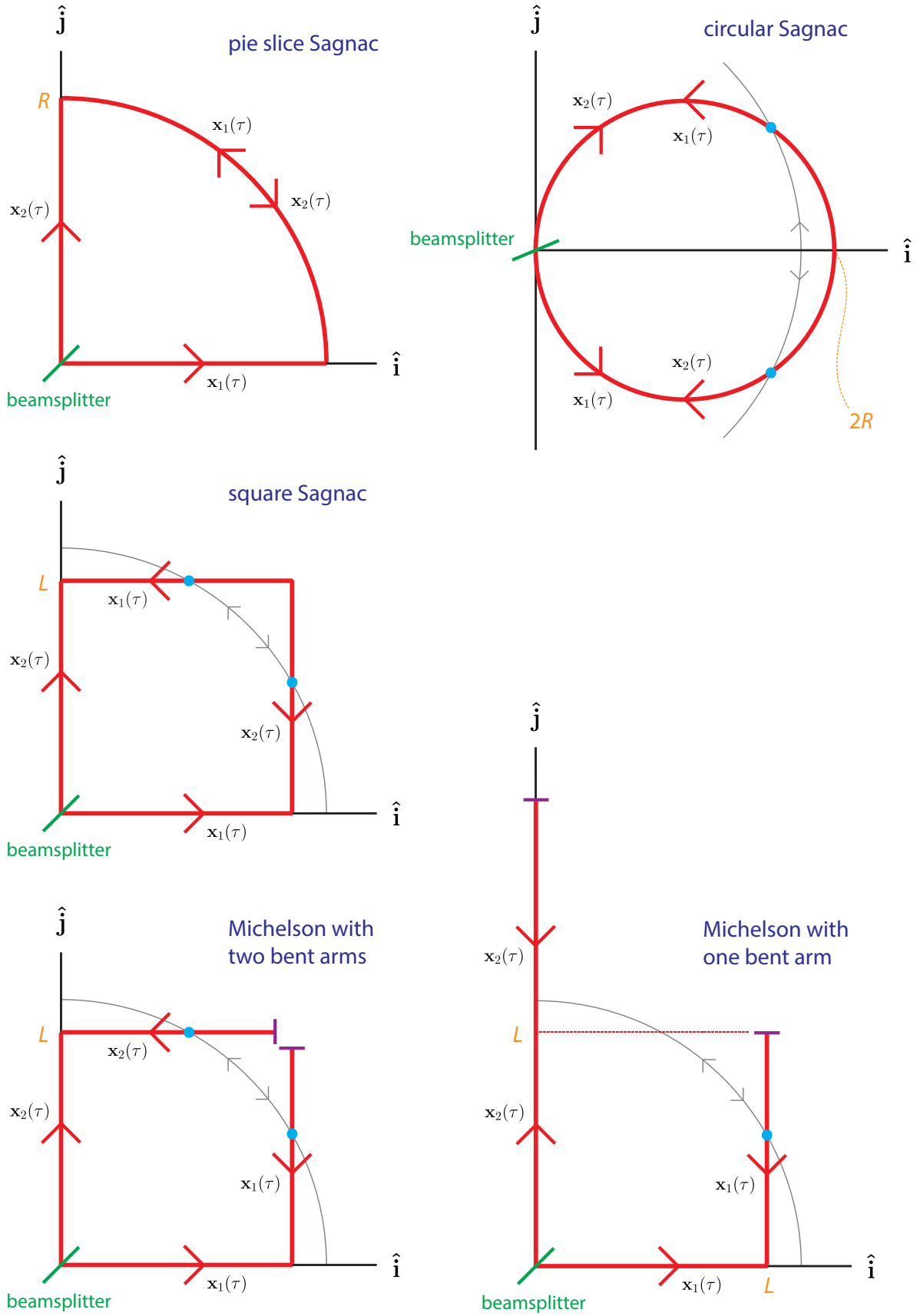


FIG. 4. Schematics of the optical paths in various interferometer setups where the light phase is sensitive to exotic rotation.

The frequency-domain PSD can easily be calculated analytically:

$$\widetilde{C}_{SS}(f | \ell_P) = 8 c \ell_P \mathcal{T}_0^2 \text{sinc}^2(\pi f \mathcal{T}_0) \quad (33)$$

The resulting spectrum is shown in Figure 5.

C. Circular Sagnac Interferometer

This is an idealized Sagnac, a circular loop of radius R with two light paths going around it in opposite directions, starting from a beamsplitter on the circumference. The geometrical coupling $\Theta(\tau)$ over the light path is a perfect sinusoidal function with one single frequency, at a system timescale equal to light circulation time $\mathcal{T}_0 = \mathcal{T} = 2\pi R/c$.

The two optical paths can be parameterized as follows (in polar coordinates, $\mathbf{x} = (r, \theta)$):

$$\mathbf{x}_a(\tau) = \left(\frac{c\mathcal{T}_0}{\pi} \sin \frac{\pi\tau}{\mathcal{T}_0}, \pi(-1)^a \left(\frac{1}{2} - \frac{\tau}{\mathcal{T}_0} \right) \right) \quad (34)$$

where $a = 1, 2$. We then calculate:

$$\Theta_a(\tau) = \hat{\boldsymbol{\theta}} \cdot \frac{\dot{\mathbf{x}}_a(\tau)}{c} = (-1)^{a-1} \sin \frac{\pi\tau}{\mathcal{T}_0} \quad (35)$$

$$\mathbb{T}(\tau', \mathbf{x}_{1,2}(\tau)) = \tau' - \frac{\mathcal{T}_0}{\pi} \sin \frac{\pi\tau}{\mathcal{T}_0} \quad (36)$$

and similar for τ'' , with $\tau = \tau'' - \tau_0$ used as the input. The inverse functions $\xi_{1,2}(\mathbb{T}, \tau_0)$ are well-defined over the entire domain, but non-analytic. The integrals for $C_{SS}(\tau_0 | \ell_P)$ and $\widetilde{C}_{SS}(f | \ell_P)$ can also only be evaluated numerically. The results are shown in Figure 5.

Notably, despite the perfectly symmetrical and sinusoidal form of the geometrical coupling, the nonlinear mapping between \mathbb{T} and τ in eq. 36 results in an asymmetric weighting over the light circulation time, because there is more accumulated fluctuation when the light path slices through more layers of future light cones per time. This asymmetric response might seem counterintuitive, but it is an important feature of the theory that is a natural consequence of the arrow of time. If one naively assumes a covariance structure that is linearly dependent on τ instead of defining \mathbb{T} on future light cones, the resulting PSD goes negative at certain frequencies, which means that it cannot represent a real-valued physical observable undergoing a wide-sense stationary random process[28].

D. Square Sagnac Interferometer

The calculations for the device response and spectra expected in a square Sagnac closely follow those of a configuration to be discussed in the next section, a Michelson interferometer with one or two arms bent 90° inward at the midpoint (see Figure 4). Since we are positing a Planckian jitter that is stochastic and covariant on light cones, the magnitude of the accumulated correlated fluctuation per optical path (1 or 2) is exactly the same for Sagnac and Michelson layouts at zero time lag τ_0 , despite the difference of a round trip versus a complete loop. The mapping between \mathbb{T} and τ is also identical (see Figure 3). The geometrical coupling $\Theta(\tau)$ differs by a sign change halfway along the light path, which does meaningfully change the behavior of the cross correlation at nonzero time lag and thereby the distribution of fluctuation power in the frequency domain. The resulting $C_{SS}(\tau_0 | \ell_P)$ and $\widetilde{C}_{SS}(f | \ell_P)$ are shown in Figure 5.

E. Bent Michelson Interferometer

It is easy to see the schematic similarities between a square Sagnac interferometer and a Michelson with both arms folded inward to form a square. The key difference is whether the light makes complete loops around the square or reflects back halfway through the light path. For the classical Sagnac effect, as in classical rotations measured with optical gyroscopes, this difference matters, because the time-symmetric round trip light path within a bent Michelson would show zero coupling to that effect. But the exotic rotational fluctuations are stochastic in time and follow the same covariance structures defined on concentric future light cones around an observer at the beamsplitter, so they

accumulate total variance at exactly the same rate in both devices, although that variance is distributed differently in time and frequency.

Sagnac interferometers have been operated many times in the past as optical gyroscopes, but not with the sensitivity required at high frequency to measure exotic rotational correlations. For technical reasons, the Holometer program plans instead to search for exotic rotational correlations with a pair of Michelson interferometers with only one bent arm. We describe this set up in more explicit detail than the other examples. We also evaluate the displayed solution for definite physical dimensions that approximate the real apparatus. One “north” arm is $2L = 39$ meters long, and the other “east” arm is bent in the middle with a folding mirror at $L = 19.5$ meters from the beamsplitter. The reference design is shown in Fig. 4. Since the straight arm has zero coupling to the effect, this device has $1/2^2$ the amount of accumulated variance observable in a Michelson with two bent arms.

Define unit vectors $\hat{\mathbf{i}}, \hat{\mathbf{j}}$ in the east and north directions respectively. Adopting a beamsplitter-centered coordinate system, the classical round-trip light paths through the east and north arms can be parameterized as

$$\mathbf{x}_1(\tau) = \begin{cases} c\tau\hat{\mathbf{i}}, & 0 < \tau < T \\ L\hat{\mathbf{i}} + (c\tau - L)\hat{\mathbf{j}}, & T < \tau < 2T \\ L\hat{\mathbf{i}} + (3L - c\tau)\hat{\mathbf{j}}, & 2T < \tau < 3T \\ (4L - c\tau)\hat{\mathbf{i}}, & 3T < \tau < 4T \end{cases} \quad \mathbf{x}_2(\tau) = \begin{cases} c\tau\hat{\mathbf{j}}, & 0 < \tau < 2T \\ (4L - c\tau)\hat{\mathbf{j}}, & 2T < \tau < 4T \end{cases} \quad (37)$$

where $T = L/c$ and the arm-segment length $L = 19.5\text{m}$. It is straightforward to calculate the geometrical couplings:

$$\Theta_1(\tau) = \hat{\boldsymbol{\theta}} \cdot \frac{\dot{\mathbf{x}}_1(\tau)}{c} = \begin{cases} 0, & 0 < \tau < T \\ \Theta_{\rightarrow}(\tau) \equiv \frac{1}{\sqrt{1+(\tau/T-1)^2}}, & T < \tau < 2T \\ \Theta_{\leftarrow}(\tau) \equiv -\frac{1}{\sqrt{1+(3-\tau/T)^2}}, & 2T < \tau < 3T \\ 0, & 3T < \tau < 4T \end{cases} \quad (38)$$

$$\Theta_2(\tau) = \hat{\boldsymbol{\theta}} \cdot \frac{\dot{\mathbf{x}}_2(\tau)}{c} = 0 \quad (39)$$

where we see that the system timescale over which the light phase is sensitive to rotational shifts is actually $\mathcal{T}_0 = 2L/c$, instead of the light circulation time $\mathcal{T} = 4L/c$. Here the arrows label the outgoing and incoming halves of the light round trip within the bent portion of the arm (the negative sign on the return half of eq. 38 is the only difference we have with the square Sagnac calculations, because there the light completes the loop in one direction).

We also derive the mapping between propagation time and beamsplitter light cone time in the bent “east” arm, shown in Figure 3:

$$\mathbb{T}(\tau'', \mathbf{x}_1(\tau'' - \tau_0)) = \begin{cases} \tau_0 & 0 < \tau'' - \tau_0 < T \\ \mathbb{T}_{\rightarrow}(\tau'', \tau_0) \equiv \tau'' - \sqrt{T^2 + (\tau'' - \tau_0 - T)^2} & T < \tau'' - \tau_0 < 2T \\ \mathbb{T}_{\leftarrow}(\tau'', \tau_0) \equiv \tau'' - \sqrt{T^2 + (\tau'' - \tau_0 - 3T)^2} & 2T < \tau'' - \tau_0 < 3T \\ \tau_0 + 2(\tau'' - \tau_0 - 2T) & 3T < \tau'' - \tau_0 < 4T \end{cases} \quad (40)$$

with a similar expression for τ' , with $\tau_0 = 0$. These can then be used to evaluate the autocovariance $C_{SS}(\tau_0 | \ell_P)$ and autospectrum $\widetilde{C}_{SS}(f | \ell_P)$, from Eqs. (25) and (30). The numerical solution is shown in Fig. 5 for $\ell_P = l_P$. A more detailed discussion of the origin of the segmented structure is given in Appendix A.

Interestingly, this spectrum has a nonzero DC response. This might seem counterintuitive, since the light path follows perfectly time-symmetric round trips (unlike in the Sagnac examples). But due to the nonlinear mapping in eq. 40, the outward trip picks up much less jitter than the portion returning inward, when the light path slices through more layers of future light cones per unit time. The fluctuations themselves average to zero, but the device response appears asymmetric. This is a consequence of the fact that the observer dependence is linked to future light cones. Since the frequency spectrum approaches a constant value at zero frequency, the mean square displacement decreases approximately linearly for averaging times longer than the apparatus size. The dominant contribution to the total displacement still comes from frequencies on the order of the free spectral range.

With Planck length normalization, the predicted signal is detectable. Assuming sensitivity similar to that already achieved with the Fermilab Holometer, a highly significant detection is expected after several hours of integration. With several hundred hours of data, the program should be able to probe an order of magnitude lower.

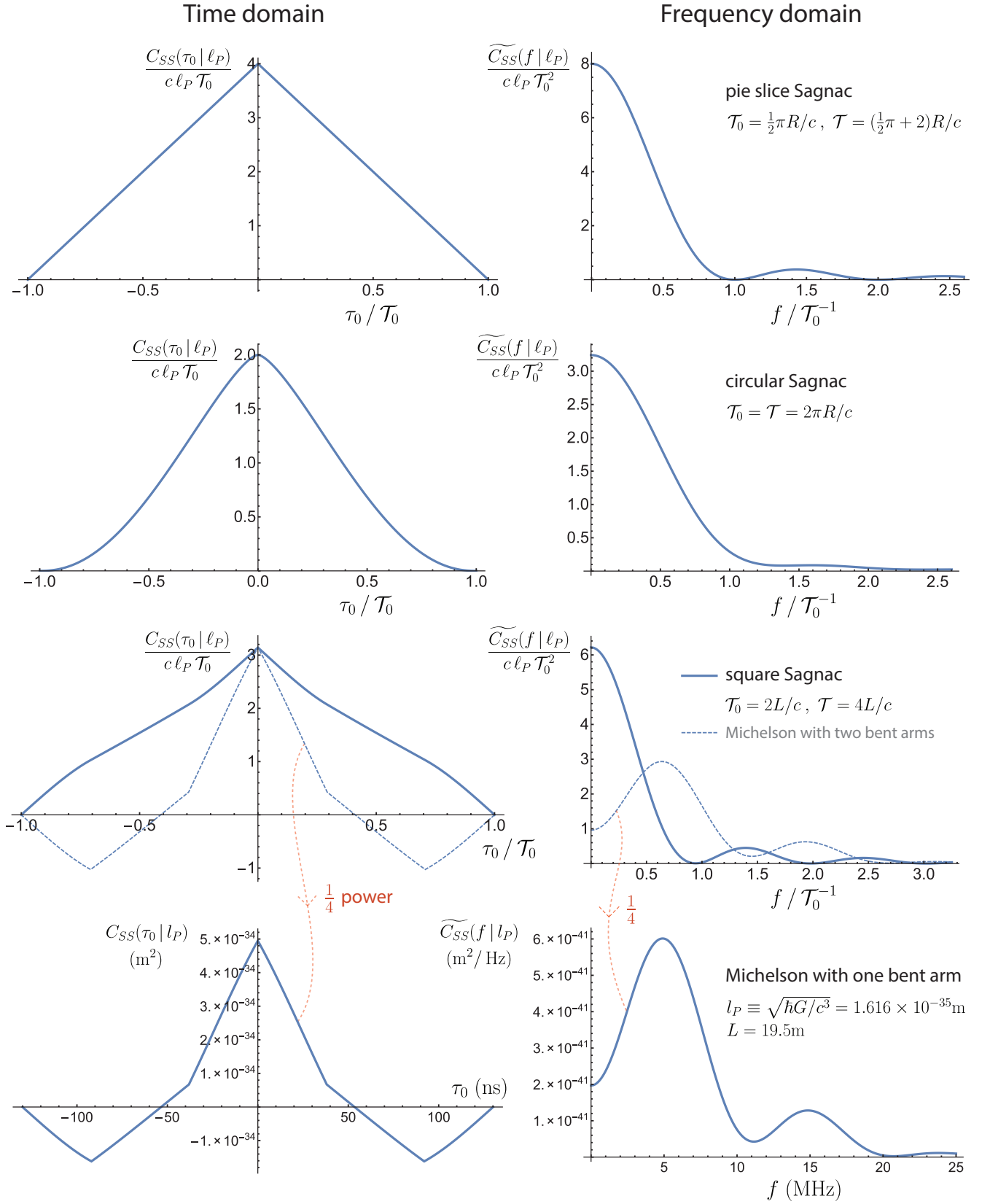


FIG. 5. The time- and frequency-domain autocovariance of signals in various interferometer setups, normalized to their system scales. For the bent Michelson, predictions in physical units are presented, with nominal standard Planck length normalization and the approximate dimensions of an experiment being commissioned. The precise coherence scale is considered a parameter to be fixed by experiment. Note locations of time domain inflections, as discussed in Appendix A. In the square Sagnac, they occur in the second derivative.

V. SPATIAL ENTANGLEMENT AND CROSS-CORRELATION

Consider a collection of tangent 2-spheres with a variety of different radii. They represent 2-sections of light cones corresponding to a variety of different observers' world lines. According to the future-light-cone covariance hypothesis, these spheres all share the same exotic phase displacement in the tangent directions, and must "choose" the same value of δX_{\perp} to collapse the Planck subsystem at their intersection point—the same projection of exotic twist onto any axis. Thus, covariance on causal boundaries appears as a sort of spooky conspiracy among many observers belonging to these light cones. How do the Planck subsystems "know about" their large scale relationships with distant observers?

The answer of course is that the relationship among quantum subsystems is always determined by the preparation and measurement of the whole state. The covariance represents entanglement, which is imposed by the assembly of subsystems into a whole system. The projection of the state is fixed by the world line of an observer. Different observers see different projections, but the whole system collapses in a self consistent way. The system is not exactly classical, but has "spooky" correlations. They appear to be nonlocal, with spacelike separations, but actually rigorously respect causal structure.

Indeed, the basic principle is that "all correlations are local": entanglement of states leads to the same transverse displacements for all events on a line with zero space time interval separation. For one observer, we have expressed this statement in terms of future light cone covariance, but the statement still applies in the case of signals cross correlated between two separate interferometers. Exotic fluctuations measured by nearly co-located interferometers are expected to exhibit a high degree of correlation. The degree of entanglement between spatial positions be can expressed in terms of the covariance structure on light cones.

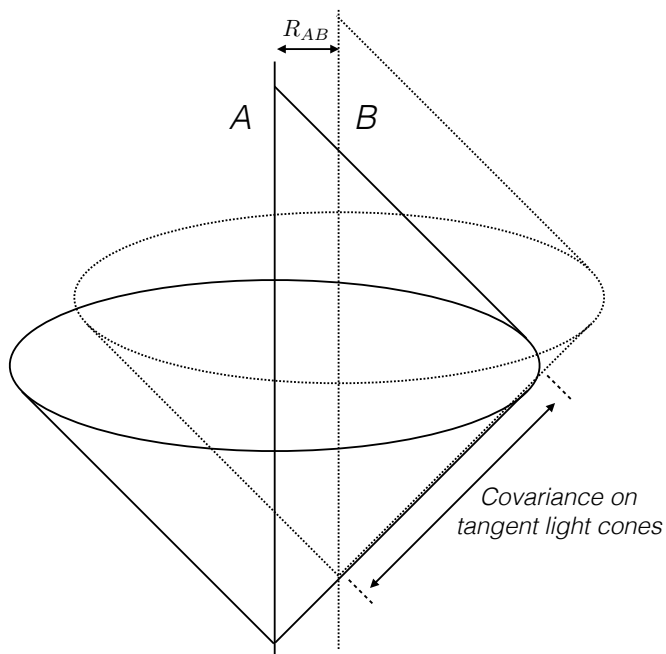


FIG. 6. The entanglement of exotic rotational displacements measured relative to two observers A and B is fixed by the in-common future tangent light cones. Along the spatial direction separating the observers, but only at laboratory time separations larger than their separation R_{AB}/c , exotic displacements for the two are the same. If the R_{AB} between beamsplitters is small compared to the region explored by their optical paths, signals of two interferometers display significant cross correlation. Thus, exotic rotational fluctuations are highly correlated in both space and time.

Consider the configuration of two observer world lines A and B , with separation R_{AB} , as illustrated in Fig. 6. The displacement rates $dX_{\perp}^{A,B}/dT_{A,B}$ are relational variables, specific to each observer and its light cone time. Covariance has been defined for future light cones of each observer, but the two sets of displacements are not independent of each other because they share the same emergent space-time. The variables refer to displacements in specific emergent directions in space: projections tangent to the radial vector to each observer. For two observers A and B , the directions agree along one line in space, the continuation of the segment separating the observers, where light cones are tangent. Along this line, transverse projections are identical at the same event in the same direction: displacements with

respect to each of the two observers agree in magnitude and direction, for events in future light cones of both (which excludes events in the interval between them, of spatial extent R_{AB} .)

This constraint determines the entanglement over the rest of the space-time. The resulting covariance can be written in terms of the two light cone times:

$$\text{cov} \left(\frac{dX_{\perp}^A}{d\mathbb{T}_A}(\mathbb{T}_A), \frac{dX_{\perp}^B}{d\mathbb{T}_B}(\mathbb{T}_B) \right) = \begin{cases} \left(\frac{\ell_P}{t_P} \right)^2, & |\mathbb{T}_A - \mathbb{T}_B| < \frac{1}{2}t_P \\ 0, & \text{otherwise} \end{cases} \quad (41)$$

Analogously to the single-interferometer case (Eq. 23), the cross-interferometer statistics of two measurement sets can now be calculated by using the covariance in Eq. (41):

$$\begin{aligned} C_{AB}(\tau_0 | \ell_P) &= \langle S_A(t) S_B(t + \tau_0) \rangle \\ &= \sum_{a,b}^{1,2} (-1)^{a+b} \left\langle \int_0^{\mathcal{T}} \frac{dX_{\perp}^A}{d\mathbb{T}_A}(\mathbb{T}_A(\tau' + (t - \mathcal{T}), \mathbf{x}_{A,a}(\tau'))) \mathcal{P}_{A,a}(\tau') d\tau' \right. \\ &\quad \left. \times \int_{\tau_0}^{\mathcal{T}+\tau_0} \frac{dX_{\perp}^B}{d\mathbb{T}_B}(\mathbb{T}_B(\tau'' + (t - \mathcal{T}), \mathbf{x}_{B,b}(\tau'' - \tau_0))) \mathcal{P}_{B,b}(\tau'' - \tau_0) d\tau'' \right\rangle \end{aligned} \quad (42)$$

Although this formula is almost the same as the autocovariance (Eq. 23), the final result differs from Eq.(26), because the separation R_{AB} enters implicitly, via the covariance and the range of integration. In laboratory time t , the agreement $\mathbb{T}_A = \mathbb{T}_B$ occurs at time offset of $|t_A - t_B| = R_{AB}/c$. This effective truncation eliminates a portion of the range of integration when evaluating the signal cross-response, which reduces the signal cross covariance below that of the autocovariance.

However, for two similar interferometers separated by a distance much smaller than their size, the non-overlapping parts of the integral due to the time offset are small compared its total value, and the cross covariance is almost equal to the autocovariance. The circle or pie slice examples illustrate this point explicitly. Consider two pie slice interferometers with a small radial displacement offset $R_{AB} = \delta R \ll R$. The offset can still be macroscopic, much larger than wavelength, beam width or even mirror size. Since the light cones are almost concentric and the projection factors are geometrically identical except for this fractionally small offset, the nonvanishing part of the correlation integral changes by only a small factor, $\delta C/C = (C_{AB} - C_A)/C_A \approx 1 - 2\delta R/R$ (see Fig. 7).

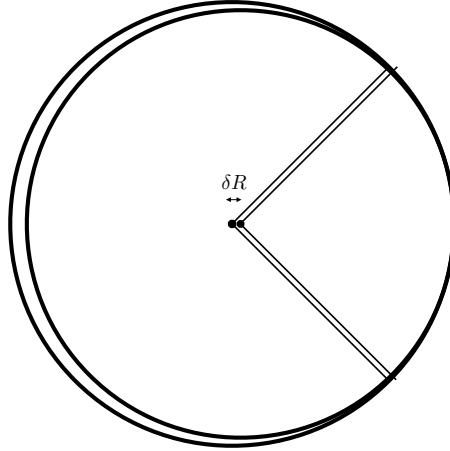


FIG. 7. Slices of two tangent light cone surfaces, with slightly separated centers, at a single time in the lab frame. Because they are tangent, the exotic transverse displacements relative to their respective centers are identical everywhere on both circles. For an offset δR much smaller than the overall scale R , the integrals that project these displacements onto neighboring pie-slice Sagnac signals (say) differ by only a small fractional amount, of the order of $\delta R/R$. Thus, the cross correlation of two machines is close to the autocorrelation, to first order in $\delta R/R$, even for macroscopic values of δR . Similarly, it is a good approximation to assume a constant displacement in the plane of the propagating wave fronts or reflecting optics, as long as they are small compared to the scale of the whole system being measured.

Thus, the signals measured by neighboring interferometers correlate in time purely due to the spatial proximity of the instruments, even if their optical paths do not coincide. This behavior makes intuitive sense: they measure the

exotic rotation of almost the same emergent space-time volume at almost the same time, in almost the same way. The exotic displacements on light cones close to the tangent cone are almost the same, because the directions to the beamsplitters at nearly the same and place nearly agree. This property is important in the design of experiments, since it allows them to take advantage of cross correlation to eliminate many spurious sources of noise and signal contamination.

VI. COMMENTS AND INTERPRETATION

A. Time Asymmetry and Decoherence

There is an apparent time asymmetry in the system we have described: the effect on a signal is not the same for outgoing and incoming parts of the same light path. The reason is simple to see: the path encounters light cones at different rates in the two directions. It is also apparent in the correlation functions, which show features at time intervals that do not correspond to the time intervals between reflections.

The asymmetry can be traced to our basic hypothesis of covariance on future and not past light cones. Physically, this choice is motivated by the preparation of the system and matching to the cosmic inertial frame. The “noise” from the Planck scale corresponds to the new information arriving from the past about the rotational frame of the distant universe. A measurement is aligned with the forward direction of time defined by quantum decoherence, which is also the direction in which entropy increases. The “collapse of the wave function” in this situation corresponds to matching with the rotation state of the rest of the universe—the reconciliation of the observer’s state with environmental information, as shown in Fig. 2. It is important to note that all of the measurable predicted correlations, as well as all of the physical elements of the system, are symmetric in time.

B. Quantum Spookiness and Emergent Time

It seems spooky, in the EPR sense, to say that a space-time itself depends on an observer and a measurement path. But in this sense, a perfectly classical, standard space-time also represents a spooky global conspiracy: the geometry of general relativity is a complete dynamical system that is independent of any observer. Here, a consistent picture emerges if we allow for appropriate causal spooky entanglements among observers. Our model of covariance formulates a specific hypothesis how macroscopic rotational relationships can emerge statistically from the Planck scale, assuming only a covariance that respects causal relationships. Nested causal surfaces of the entangled system resemble the intricately interlocked gears of a clockwork (as in Fig. 7). Tangent displacements at causal boundaries agree at every point for all of the nested causal diamonds at that point. All observers can agree about physical observables, because all exotic “motions” are defined in terms of radial light propagation and have no effect on radially propagating phase. This consistency also ensures that the whole system closely resembles a continuous classical geometry on large scales. A path in space that begins and ends on an observer’s world line provides an operational definition of an inertial frame, built statistically out of relationships among quantum elements at the Planck scale.

A well known feature of relational quantum geometry is that time itself is also part of the quantum system. This issue has been avoided in the analysis above by analyzing the exotic motion in an observer’s inertial frame, and covariance on Lorentz invariant light cones. For a single world line, light phase along any radial direction represents a perfect “light cone time” clock. But for two separate world lines, their clock phases only agree for light propagating along the radial separation between them. There are differences in the transverse phase, which can be visualized as due an exotic transverse “movement without motion” of the underlying space at each world line relative to the other that causes a Planck scale random drift of transversely oriented light clocks. In this sense, emergent time is not separate from position, but also displays quantum weirdness.

C. Relation to Gravity

It is well known that gravity creates a quantum catastrophe in the ultraviolet: Wheeler’s “quantum foam,” a chaotic roiling state of virtual black holes. Many of those problems have been addressed by UV completions of field theory, but as discussed above, quantum foam also creates problems in the infrared associated with rotation[16]: in quantum foam, the local inertial frame is a superposition of states with a natural rotational indeterminacy at the Planck frequency. The model here addresses those problems in a systematic way. However, our statistical model has

been formulated entirely around inertial frames in a flat space-time, and has not addressed the issue of emergent curvature.

The covariance imposed here reduces the number of independent degrees of freedom. As discussed in earlier work[10–16], the information scales as the area of a causal boundary in Planck units. Thus, the model agrees with holographic entropy estimates from semiclassical quantum gravity[29–34] and loop quantum gravity[1–3], and entangles virtual field states[35] enough to reconcile them with gravity on large scales. By construction, the exotic degrees of freedom posited here live on causal surfaces, so they are compatible with a flat-space limit of quantum gravity, and fit well with a thermodynamic theory of emergent curvature[32]. A complete theory that addresses these issues would of course require generalization to accelerated observers and curved space-time.

ACKNOWLEDGMENTS

We are grateful for much encouragement and challenging discussion from other members of the Holometer team. This work was supported by the John Templeton Foundation, and by the Department of Energy at Fermilab under Contract No. DE-AC02-07CH11359.

-
- [1] C. Rovelli, *Quantum Gravity* (Cambridge University Press, 2004).
 - [2] T. Thiemann, *Modern Canonical Quantum General Relativity* (Cambridge University Press, 2008) arXiv:gr-qc/0110034 [gr-qc].
 - [3] A. Ashtekar, PoS **QGQGS2011**, 001 (2011), arXiv:1201.4598 [gr-qc].
 - [4] S. Weinberg, *The Quantum Theory of Fields* (Cambridge University Press, 1996).
 - [5] F. Wilczek, Rev. Mod. Phys. **71**, S85 (1999).
 - [6] T. Mohaupt, in *Quantum Gravity: From Theory to Experimental Search*, Lecture Notes in Physics, Vol. 631, edited by D. Giulini, C. Kiefer, and C. Lämmerzahl (Springer, Berlin; New York, 2003) pp. 173–251, arXiv:hep-th/0207249.
 - [7] J. Polchinski, *String Theory* (Cambridge University Press, 1998).
 - [8] J. H. Schwarz, “Introduction to superstring theory,” (2000), arXiv:hep-ex/0008017.
 - [9] M. R. Douglas and N. A. Nekrasov, Rev. Mod. Phys. **73**, 977 (2001).
 - [10] O. Kwon and C. J. Hogan, Class. Quant. Grav. **33**, 105004 (2016), arXiv:1410.8197 [gr-qc].
 - [11] C. J. Hogan, Phys. Rev. **D77**, 104031 (2008).
 - [12] C. J. Hogan, Phys. Rev. **D78**, 087501 (2008).
 - [13] C. J. Hogan, Phys. Rev. **D85**, 064007 (2012).
 - [14] C. Hogan, in *9th LISA Symposium*, Astronomical Society of the Pacific Conference Series, Vol. 467, edited by G. Auger, P. Binétruy, and E. Plagnol (2013) p. 17, arXiv:1208.3703 [quant-ph].
 - [15] C. J. Hogan and O. Kwon, (2015), arXiv:1506.06808 [gr-qc].
 - [16] C. Hogan, (2015), arXiv:1509.07997 [gr-qc].
 - [17] R. Lieu and L. W. Hillman, ApJ **585**, L77 (2003), astro-ph/0301184.
 - [18] Y. J. Ng, W. A. Christiansen, and H. van Dam, ApJ **591**, L87 (2003), astro-ph/0302372.
 - [19] R. Ragazzoni, M. Turatto, and W. Gaessler, ApJ **587**, L1 (2003), astro-ph/0303043.
 - [20] W. A. Christiansen, Y. J. Ng, and H. van Dam, Physical Review Letters **96**, 051301 (2006), gr-qc/0508121.
 - [21] W. A. Christiansen, Y. J. Ng, D. J. E. Floyd, and E. S. Perlman, Phys. Rev. D. **83**, 084003 (2011), arXiv:0912.0535 [astro-ph.CO].
 - [22] E. S. Perlman, Y. J. Ng, D. J. E. Floyd, and W. A. Christiansen, A&A **535**, L9 (2011), arXiv:1110.4986.
 - [23] E. S. Perlman, S. A. Rappaport, W. A. Christiansen, Y. J. Ng, J. DeVore, and D. Pooley, ApJ **805**, 10 (2015), arXiv:1411.7262.
 - [24] A. S. Chou *et al.*, (2015), arXiv:1512.01216 [gr-qc].
 - [25] R. X. Adhikari, Reviews of Modern Physics **86**, 121 (2014), arXiv:1305.5188 [gr-qc].
 - [26] E. J. Post, Rev. Mod. Phys. **39**, 475 (1967).
 - [27] K. U. Schreiber, A. Gebauer, H. Igel, J. Wassermann, R. B. Hurst, and J.-P. R. Wells, Comptes Rendus Physique **15**, 859 (2014), the Sagnac effect: 100 years later / L’effet Sagnac : 100 ans après.
 - [28] A. Oppenheim and G. Verghese, *Signals, Systems and Inference, Global Edition* (Pearson Education, Limited, 2016).
 - [29] G. ’t Hooft, , 0284 (1993), arXiv:gr-qc/9310026 [gr-qc].
 - [30] L. Susskind, J. Math. Phys. **36**, 6377 (1995).
 - [31] R. Bousso, Rev.Mod.Phys. **74**, 825 (2002), arXiv:hep-th/0203101 [hep-th].
 - [32] T. Jacobson, Phys. Rev. Lett. **75**, 1260 (1995).
 - [33] E. Verlinde, JHEP **1104**, 029 (2011).
 - [34] T. Padmanabhan, Gen. Rel. Grav. **46**, 1673 (2014), arXiv:1312.3253 [gr-qc].
 - [35] A. G. Cohen, D. B. Kaplan, and A. E. Nelson, Phys. Rev. Lett. **82**, 4971 (1999).

Appendix A: Detailed Analysis of the Bent Michelson Configuration

The simple setup of the experiment design chosen for this example allows a detailed set of analytical expressions for the integrals along each segment, as explicitly shown in this appendix. Starting with Eqs. (38) and (39), we see that the light propagation has a nonzero angular component only along the “bent” portion of the east arm. From this point on, we drop the subscripts 1 and 2 for the two arms, and only carry out calculations over the east arm (using $\mathbf{x}_1(\tau)$ and $\Theta_1(\tau)$ above). So,

$$C_{SS}(\tau_0 | \ell_P) = \int_0^{4T} d\tau' \frac{d\mathbb{T}}{d\tau'}(\tau', \mathbf{x}(\tau')) \Theta(\tau') \int_{\tau_0}^{4T+\tau_0} d\tau'' \frac{d\mathbb{T}}{d\tau''}(\tau'', \mathbf{x}(\tau'' - \tau_0)) \Theta(\tau'' - \tau_0) \times \left\langle \frac{dX_{\perp}}{d\mathbb{T}}(\mathbb{T}(\tau', \mathbf{x}(\tau'))) \frac{dX_{\perp}}{d\mathbb{T}}(\mathbb{T}(\tau'', \mathbf{x}(\tau'' - \tau_0))) \right\rangle \quad (\text{A1})$$

where $\mathbf{x}(\tau) = \mathbf{x}_1(\tau)$ and $\Theta(\tau) = \Theta_1(\tau)$.

From eq. 40, we derive inverse functions of $\mathbb{T}_{\rightarrow}(\tau'', \tau_0)$ and $\mathbb{T}_{\leftarrow}(\tau'', \tau_0)$, as follows:

$$\tau'' = \xi_{\rightarrow}(\mathbb{T}, \tau_0) \equiv \frac{1}{2} \left(\frac{T^2}{T + \tau_0 - \mathbb{T}} + T + \tau_0 + \mathbb{T} \right) \quad (\text{A2})$$

$$\tau'' = \xi_{\leftarrow}(\mathbb{T}, \tau_0) \equiv \frac{1}{2} \left(\frac{T^2}{3T + \tau_0 - \mathbb{T}} + 3T + \tau_0 + \mathbb{T} \right) \quad (\text{A3})$$

Again, similar equations hold for τ' , with $\tau_0 = 0$. These inverse functions do not hold over the entire light paths, but in the ranges $T < \tau' < 3T$ and $T < \tau'' - \tau_0 < 3T$ where the geometrical coupling is nonzero, they are well-defined.

We use the following notation for the projection factors:

$$\mathcal{P}_{\rightarrow}(\tau) \equiv \left[\frac{d\mathbb{T}_{\rightarrow}}{d\tau}(\tau, 0) \right] \Theta_{\rightarrow}(\tau) \quad \text{and} \quad \mathcal{P}_{\leftarrow}(\tau) \equiv \left[\frac{d\mathbb{T}_{\leftarrow}}{d\tau}(\tau, 0) \right] \Theta_{\leftarrow}(\tau) \quad (\text{A4})$$

We now have the tools to evaluate eq. A1, the autocovariance of the signal for a layout that approximates an experiment now under construction.

Evaluating $C_{SS}(\tau_0 | \ell_P)$ is best done in segments. We know $C_{SS}(\tau_0 | \ell_P)$ is symmetric, so we will consider positive values of τ_0 without any loss of generality. Figure 3 is a schematic representation of eq. 40, showing light cone slices of \mathbb{T} versus the radial axis $|\mathbf{x}(\tau)|$, where $\tau = \tau'$ and $\tau = \tau'' - \tau_0$ for the two tracer photon trajectories separated by time lag τ_0 . We see that $\mathbb{T}(\tau', \mathbf{x}(\tau'))$ or $\mathbb{T}(\tau'', \mathbf{x}(\tau'' - \tau_0)) - \tau_0$ stays at 0 until the bend mirror ($\tau = T$), runs to $(2 - \sqrt{2})T$ at the end mirror reflection ($\tau = 2T$), and then to $2T$ at the bend mirror on the way back ($\tau = 3T$).

Following the covariance structure, the integrals should be performed over the range of time where there are future light cones commonly intersected by both tracer photon paths, within the constraints $T < \tau' < 3T$ and $T < \tau'' - \tau_0 < 3T$. These integrals should be subdivided into separate segments whenever either tracer photon path flips from outgoing to incoming, at $\tau = 2T$. Converting the integrals into intervals in \mathbb{T} , we see that it should be performed between τ_0 and $2T$, with segment divisions at $(2 - \sqrt{2})T$ and $\tau_0 + (2 - \sqrt{2})T$.

Correlations between segments in the same direction (outgoing or incoming) give positive contributions to the integral, but anti-correlations between outgoing and incoming segments give negative ones. This sharp discontinuity in geometrical coupling at the end mirror reflection gives rise to inflections in the autocorrelation whenever a segment division is eliminated by increases in time lag τ_0 (see Figure 5). This is a feature not seen in the square Sagnac spectra—although the mirror reflections happen at roughly the same points, the geometrical coupling is continuous there.

The functional support for $C_{SS}(\tau_0 | \ell_P)$ divides into the following three ranges, making clear the origin of these features:

i) $0 < \tau_0 < (2 - \sqrt{2})T$

$C_{SS}(\tau_0 | \ell_P)$

$$\begin{aligned}
&= \int_{\xi_{\rightarrow}(\tau_0, 0)}^{2T} d\tau' \mathcal{P}_{\rightarrow}(\tau') \int_{T+\tau_0}^{\xi_{\rightarrow}((2-\sqrt{2})T, \tau_0)} d\tau'' \mathcal{P}_{\rightarrow}(\tau'' - \tau_0) \times \left\langle \frac{dX_{\perp}}{d\mathbb{T}}(\mathbb{T}_{\rightarrow}(\tau', 0)) \frac{dX_{\perp}}{d\mathbb{T}}(\mathbb{T}_{\rightarrow}(\tau'', \tau_0)) \right\rangle \\
&+ \int_{2T}^{\xi_{\leftarrow}(\tau_0+(2-\sqrt{2})T, 0)} d\tau' \mathcal{P}_{\leftarrow}(\tau') \int_{\xi_{\leftarrow}((2-\sqrt{2})T, \tau_0)}^{2T+\tau_0} d\tau'' \mathcal{P}_{\rightarrow}(\tau'' - \tau_0) \times \left\langle \frac{dX_{\perp}}{d\mathbb{T}}(\mathbb{T}_{\leftarrow}(\tau', 0)) \frac{dX_{\perp}}{d\mathbb{T}}(\mathbb{T}_{\rightarrow}(\tau'', \tau_0)) \right\rangle \\
&+ \int_{\xi_{\leftarrow}(\tau_0+(2-\sqrt{2})T, 0)}^{3T} d\tau' \mathcal{P}_{\leftarrow}(\tau') \int_{2T+\tau_0}^{\xi_{\leftarrow}(2T, \tau_0)} d\tau'' \mathcal{P}_{\leftarrow}(\tau'' - \tau_0) \times \left\langle \frac{dX_{\perp}}{d\mathbb{T}}(\mathbb{T}_{\leftarrow}(\tau', 0)) \frac{dX_{\perp}}{d\mathbb{T}}(\mathbb{T}_{\leftarrow}(\tau'', \tau_0)) \right\rangle \quad (\text{A5})
\end{aligned}$$

$$\begin{aligned}
&= c \ell_P \int_{\tau_0}^{(2-\sqrt{2})T} \Theta_{\rightarrow}(\xi_{\rightarrow}(\mathbb{T}, 0)) \Theta_{\rightarrow}(\xi_{\rightarrow}(\mathbb{T}, \tau_0) - \tau_0) d\mathbb{T} \\
&+ c \ell_P \int_{(2-\sqrt{2})T}^{\tau_0+(2-\sqrt{2})T} \Theta_{\leftarrow}(\xi_{\leftarrow}(\mathbb{T}, 0)) \Theta_{\rightarrow}(\xi_{\rightarrow}(\mathbb{T}, \tau_0) - \tau_0) d\mathbb{T} \\
&+ c \ell_P \int_{\tau_0+(2-\sqrt{2})T}^{2T} \Theta_{\leftarrow}(\xi_{\leftarrow}(\mathbb{T}, 0)) \Theta_{\leftarrow}(\xi_{\leftarrow}(\mathbb{T}, \tau_0) - \tau_0) d\mathbb{T} \quad (\text{A6})
\end{aligned}$$

ii) $(2 - \sqrt{2})T < \tau_0 < \sqrt{2}T$

$C_{SS}(\tau_0 | \ell_P)$

$$\begin{aligned}
&= \int_{\xi_{\leftarrow}(\tau_0, 0)}^{\xi_{\leftarrow}(\tau_0+(2-\sqrt{2})T, 0)} d\tau' \mathcal{P}_{\leftarrow}(\tau') \int_{T+\tau_0}^{2T+\tau_0} d\tau'' \mathcal{P}_{\rightarrow}(\tau'' - \tau_0) \times \left\langle \frac{dX_{\perp}}{d\mathbb{T}}(\mathbb{T}_{\leftarrow}(\tau', 0)) \frac{dX_{\perp}}{d\mathbb{T}}(\mathbb{T}_{\rightarrow}(\tau'', \tau_0)) \right\rangle \\
&+ \int_{\xi_{\leftarrow}(\tau_0+(2-\sqrt{2})T, 0)}^{3T} d\tau' \mathcal{P}_{\leftarrow}(\tau') \int_{2T+\tau_0}^{\xi_{\leftarrow}(2T, \tau_0)} d\tau'' \mathcal{P}_{\leftarrow}(\tau'' - \tau_0) \times \left\langle \frac{dX_{\perp}}{d\mathbb{T}}(\mathbb{T}_{\leftarrow}(\tau', 0)) \frac{dX_{\perp}}{d\mathbb{T}}(\mathbb{T}_{\leftarrow}(\tau'', \tau_0)) \right\rangle \quad (\text{A7})
\end{aligned}$$

$$\begin{aligned}
&= c \ell_P \int_{\tau_0}^{\tau_0+(2-\sqrt{2})T} \Theta_{\leftarrow}(\xi_{\leftarrow}(\mathbb{T}, 0)) \Theta_{\rightarrow}(\xi_{\rightarrow}(\mathbb{T}, \tau_0) - \tau_0) d\mathbb{T} \\
&+ c \ell_P \int_{\tau_0+(2-\sqrt{2})T}^{2T} \Theta_{\leftarrow}(\xi_{\leftarrow}(\mathbb{T}, 0)) \Theta_{\leftarrow}(\xi_{\leftarrow}(\mathbb{T}, \tau_0) - \tau_0) d\mathbb{T} \quad (\text{A8})
\end{aligned}$$

iii) $\sqrt{2}T < \tau_0 < 2T$

$C_{SS}(\tau_0 | \ell_P)$

$$= \int_{\xi_{\leftarrow}(\tau_0, 0)}^{3T} d\tau' \mathcal{P}_{\leftarrow}(\tau') \int_{T+\tau_0}^{\xi_{\leftarrow}(2T, \tau_0)} d\tau'' \mathcal{P}_{\rightarrow}(\tau'' - \tau_0) \times \left\langle \frac{dX_{\perp}}{d\mathbb{T}}(\mathbb{T}_{\leftarrow}(\tau', 0)) \frac{dX_{\perp}}{d\mathbb{T}}(\mathbb{T}_{\rightarrow}(\tau'', \tau_0)) \right\rangle \quad (\text{A9})$$

$$= c \ell_P \int_{\tau_0}^{2T} \Theta_{\leftarrow}(\xi_{\leftarrow}(\mathbb{T}, 0)) \Theta_{\rightarrow}(\xi_{\rightarrow}(\mathbb{T}, \tau_0) - \tau_0) d\mathbb{T} \quad (\text{A10})$$